Nanoscale

Ligand dynamics control structure, elasticity, and high-pressure behavior of nanoparticle superlattices

Journal:	*Nanoscale*
Manuscript ID	NR-ART-12-2018-009699.R1
Article Type:	Paper
Date Submitted by the Author:	05-Feb-2019
Complete List of Authors:	Patra, Tarak; Argonne National Laboratory, Center for Nanoscale Materials Chan, Henry; Argonne National Laboratory, Podsiadlo, Paul; Argonne National Laboratory, Center for Nanoscale Materials Shevchenko, Elena; Argonne National Laboratory, Center for Nanoscale Materials Sankaranarayanan, Subramanian; Argonne National laboratory, Center for Nanoscale Materials Narayanan, Badri; Argonne National laboratory, Materials Science Division; University of Louisville, Department of Mechanical Engineering

Ligand dynamics control structure, elasticity, and high-pressure behavior of nanoparticle superlattices

Tarak K. Patra,[1] Henry Chan,[1] Paul Podsiadlo,[1] Elena V. Shevchenko,[1*] Subramanian KRS Sankaranarayanan,[1*] and Badri Narayanan[2,3*]

[1]Center for Nanoscale Materials, Argonne National Laboratory, Argonne, IL 60439
[2]Materials Science Division, Argonne National Laboratory, Argonne, IL 60439
[3]Department of Mechanical Engineering, University of Louisville, Louisville, KY 40292

Abstract

Precise engineering of nanoparticle superlattices (NPSLs) for energy applications requires a molecular-level understanding of the physical factors governing their morphology, periodicity, mechanics, and response to external stimuli. Such knowledge, particularly the impact of ligand dynamics on physical behavior of NPSLs, is still in its infancy. Here, we combine coarse-grained molecular dynamics simulations, and small angle X-ray scattering experiments in diamond anvil cell to demonstrate that coverage density of capping ligands (i.e., number of ligands per unit area of a nanoparticle's surface), strongly influences the structure, elasticity, and high-pressure behavior of NPSLs using face-centered cubic PbS-NPSLs as a representative example. We demonstrate that ligand coverage density dictates (a) the extent of diffusion of ligands over NP surfaces, (b) spatial distribution of the ligands in the interstitial spaces between neighboring NPs, and (c) the fraction of ligands that interdigitate across different nanoparticles. We find that below a critical coverage density (1.8 nm^{-2} for 7 nm PbS NPs capped with oleic acid), NPSLs collapse to form disordered aggregates via sintering, even under ambient conditions. Above the threshold ligand coverage density, NPSLs surprisingly preserve their crystalline order even under high applied pressures (~ 40 - 55 GPa), and show a completely reversible pressure behavior. This opens the possibility of reversibly manipulating lattice spacing of NPSLs, and in turn, finely tuning their collective electronic, optical, thermo-mechanical, and magnetic properties.

Keywords: Nanoparticle superlattices, molecular dynamics, ligand distribution, ligand interdigitation, reversible pressure behavior

Corresponding Authors

*E-mail: badri.narayanan@louisville.edu (B.N)
*E-mail: skrssank@anl.gov (S.K.R.S.S)
*E-mail: eshevchenko@anl.gov (E.V.S)

1. Introduction

Advances in scalable self-assembly strategies have enabled synthesis of highly ordered arrays of ligand-stabilized colloidal nanoparticles (NPs), termed nanoparticle superlattices (NPSLs), with exceptional thermal,[1] mechanical,[2] electronic,[3] and optical[4] properties. For instance, precise ordering of NPs into NPSLs has led to several technologically relevant phenomena, including, metal-to-insulator transition,[5] vibrational coherence,[6] enhanced *p*-type conductivity,[7] ferro-/ferri-magnetism,[8–10] novel plasmonic properties,[11] spin-dependent electron transport,[12] and superior thermal behavior.[1] Such unique set of physical properties make NPSLs promising for numerous optoelectronics, energy harvesting, and sensing applications.[13–15] The presence of soft ligands also opens up a unique opportunity to finely tune the collective properties of NPSLs. Even for a chosen combination of NP and capping ligands, the electronic, optical, and magnetic coupling between NPs can be precisely controlled by varying the distance between NPs;[16–19] e.g., reversible metal-to-insulator transition can be achieved in 2D silver NPSLs by varying NP-NP separations.[5] Numerous methods, including ligand replacement,[3,20] pressure,[18] and thermal treatment after assembly,[21] have reported success in tuning the inter-NP distance. Among these, applied pressure is particularly lucrative to achieve desired NP-NP distances over a wide range, since NPSLs can withstand high pressures (tens of GPa) without losing their long-range order, and pressure-induced structural changes can be completely reversed.[16] In addition, NPSLs have been reported to be mechanically robust, with elastic stiffness similar to those of lightweight structural composites (~10 GPa);[2,22,23] this further makes applied pressure a suitable route to control the collective properties of NPSL.

Manipulation of the interparticle spacing in NPSLs *via* applied external pressure is a straightforward approach to tune physical properties of such structures. In few previous studies, compression of NP assemblies have been found to accompany sintering of individual NPs; [23,24] this phenomenon can be used to engineer nanostructures with specific morphologies.[25] Importantly, assemblies of oleic acid modified PbS NPs synthesized in different research groups have sometimes led to structurally stable superlattices, while other times the individual NPs are found to sinter.[16,23] The underlying molecular level picture of these seemingly disparate observations remains largely unknown. While a broad range of NPs have been assembled into three-dimensional NPSLs, understanding of the origin of structural stability, mechanical

properties and high-pressure behavior of these hybrid materials consisting of "hard" inorganic cores and "soft" organic ligands at molecular level is still in its infancy.[1,2,15,26–28] Previous reports indicate that structure, and mechanics of NPSLs are primarily controlled by weak dispersive forces (e.g., van der Waals, hydrogen bonding etc.) and packing entropy of ligands of different NPs.[1,28–30] Moreover, varying packing densities can modify surface organization of ligands and modify surface energies. This can cause the transition of driving force for self-assembly from entropy maximization to reduction of overall free energy; and, in turn, lead to various ordered morphologies that are not possible to achieve *via* entropic factors alone. [31–33] Consistent with these claims, recent electron microscopy, and nano-indentation studies demonstrate that NPSLs exhibit superior mechanical properties even in the absence of chain entanglement or cross-linking, and slight structural disorder.[2] Also the packing geometry, structural conformation of ligands, and the mobility of ligands on the surface of nanoparticles are also known to impact mechanical cohesion in NPSLs, and their response to applied pressure.[13,34] Furthermore, our previous works on Au NPSLs have shown that their thermo-mechanical properties are strongly influenced by inter-digitation of ligands, as well as the spatial arrangement of ligands between neighboring NPs.[1] Other *in situ* small angle X-ray scattering (SAXS) studies using diamond anvil cell (DAC) indicate that under applied pressure, the structure of NPSLs evolve via elastic response of ligands, ligand compression, ligand detachment, and deviatoric compression of ligands between different NPs.[26] Despite these findings, the role played by molecular scale dynamics of ligands in governing structural, mechanical, and pressure behavior of NPs, as well as their correlation with ligand coverage densities are still not fully understood. Therefore, the fundamental knowledge of ligand dynamics and its connection to assembly process, sintering of NPs and thermo-mechanical properties of NPLSs is not only crucial for gaining precise control over the physical properties of NPSLs, but is also essential to design pathways to synthesize these hybrid crystals with desired crystallinity. For instance, minor changes in synthesis protocols, e.g., washing schemes can effectively alter the ligand coverage,[26,35] which in turn impacts the morphology, symmetry, dimensionality, and thermo-mechanical behavior of the self-assembled NPSLs.[24,36]

Here, we combine coarse-grained molecular dynamics (CGMD) simulations, and SAXS experiments in diamond anvil cell (DAC) to explore the dynamic processes at the molecular level. We show that structural response of NPSLs to applied pressure, their mechanical

properties, as well as NP-NP spacing are strongly correlated with the surface mobility of ligands, their spatial distribution between neighboring NPs, and the extent of ligand-interdigitation. We demonstrate that a certain critical density of ligand coverage on the constituent NPs is required to form stable NPSLs. Below this density (such as that possible due to extensive washing[27]), NPSLs tend to collapse often under ambient conditions resulting in disordered aggregates of NPs via sintering. Above the critical coverage, NPSLs preserve their crystalline order even up to high applied pressures (~40 GPa); more importantly, the pressure-induced changes in NP-NP spacing are completely recovered upon release, without any noticeable hysteresis. We attribute this absence of hysteresis to the reversible nature of inter-digitation between ligands of neighboring NPs; essentially, we find that applied pressure impacts the fraction of ligands involved in inter-digitation, while the relative orientation of the ligands between neighboring NPs remains constant. Furthermore, ligand coverage also dictates the propensity of a ligand to inter-digitate with or deflect away from ligands on neighboring NPs, which, in turn, governs the mechanical behavior of NPSLs. In ligand-deficient NPSLs (with coverage above critical value), ligands predominantly inter-digitate, while in the ligand-rich cases, deflection of ligands is more prevalent. Our CGMD simulations unambiguously indicate that ligand-deflection significantly enhances the elastic stiffness of NPSL.

2. Materials and methods

Synthesis and characterization. The PbS NPs (of size 7 nm) are synthesized using the method of Hines and Scholes.[37] Subsequently, these PbS NPs are assembled into FCC superlattices via a controlled oversaturation technique as described in our previous work.[16,38] Typically, a single Si strip is placed vertically in a glass test tube containing a solution of NPs in toluene (with 0.2 mg of PbS NPs). Subsequently, we add 1.5 mL of isopropanol (non-solvent) to slowly destabilize the NP solution over a period of ~ 1 week; thereafter, the substrates containing the NPSLs are removed, and air-dried. Thermogravimetric (TGA) analysis was performed with a Mettler-Toledo STAR^e TGA/SDTA851^e system operated under inert, N_2 atmosphere. The NPSLs were scratched from the Si substrate and placed into the Al boat.

Among the synthesized NPSLs, we chose few representative ones with dimensions compatible with DAC to characterize the pressure response of NPSL. In each high-pressure experiment, only one individual NPSL (~30 microns) is loaded into a ~150 μm-diameter hole in a pre-indented Re

gasket[16]. The NPSL was loaded manually under the optical microscope by picking it from the glass substrate using the sharp wood needle. The pressure is monitored spectroscopically via measuring the fluorescence peak position of ruby fluorescent microsphere, loaded alongside with the NPSL. Neon (Ne) is loaded to the DAC as a pressure-transmitting medium using a pressurized gas loading system. The synchrotron small angle X-ray scattering techniques (sector 12, Advanced Photon Source) in combination with a diamond anvil cell (DAC) technique are used to monitor the structural evolution of NPSLs.[39] For these X-ray experiments, a monochromatic beam (energy, 12 keV corresponding to X-ray wavelength λ =1.0332 Å) is focused onto an area of 100 μm x 50 μm on the sample at a sample-to-detector distance of ~2 m. An APS built CCD detector is employed for the in situ SAXS experiments. Scanning electron microscopy is conducted using JEOL 7500F, while transmission electron microscopy images are captured using JEOL 2100F.

Materials. Isopropanol, toluene, oleic acid, and bis(trimethylsilyl) sulfide ($(TMS)_2S$) are purchased from Sigma-Aldrich with at least ACS purity. $PbAc_2{\bullet}3H_2O$ is obtained from Across Chemicals. We purchased polished Si (100) wafers from Silicon Quest International (Santa Clara, CA) for growing NPSLs; these wafers are diced into 4 mm by 1 cm strips with a dicing saw and further cleaned by sonication in pure toluene. Glass test tubes (0.8 cm i.d., by 10 cm long) used for NPSL assembly are purchased from Fisher Scientific. For DAC chamber, diamonds are purchased from Almax Industries, while rhenium foil is purchased from Sigma-Aldrich. This foil is diced into 4 mm × 4 mm squares for use as gasket chambers.

Coarse-grained molecular dynamics simulations. Fundamental understanding of the structural stability, elasticity, and high-pressure behavior of NPSLs require large computational superlattice composed of several million atoms. Molecular dynamics simulations based on all-atom models for such large systems (with multiple initial configurations) over several tens of nanoseconds are computationally intractable. Therefore, we turn to atomistic-informed MARTINI[40] coarse grained model of PbS NPs ligated with oleic acid ligands. The MARTINI framework provides sufficient coarse-graining while retaining the chemical description of fatty acids among other typical ligands.[41] Such coarse-grained models have shown great success in describing ligand dynamics, and its impact on structural, thermal, and mechanical properties of self-assembled nanoparticle superstructures[1,35,42] In this framework, the PbS-NP core is

represented by an indivisible bead (type NP), while each oleic acid is modelled by a string of six beads bonded to each other (Supplementary Information, Figure S1); one of the terminal beads of the oleic acid is attached to the PbS nanoparticle core via a harmonic bond. All non-bonded interactions between the beads are modelled using Lennard-Jones potentials (See Figure S1c for parameters employed in this work). Note that the oleic acid ligands are allowed to move over the surface of the nanoparticle to which they are tethered. We also note that the MARTINI CG model used in this work distinguishes C=C and C-C bonds, and captures the effect of C=C bond on rigidity of oleic acid ligands (See Supporting Information, Figure S1). This is particularly important since the increased rigidity owing to C=C has been reported to influence extent of ligand interdigitation. [33]

First, we generate all-atom configurations for oleic acid ligands that are randomly distributed on a PbS NP bead at various ligand coverages ρ (number of ligand molecules per unit surface area of NP), with values ranging from 0.7nm^{-2} to 5.5nm^{-2}. The all-atom configurations are then coarse-grained in accordance to MARTINI framework (Figure S1); the ligated coarse-grained models at various ligand coverages are, subsequently, equilibrated at 300 K for 10 ns. At each ρ, we build NPSLs with face-centered cubic symmetry using the equilibrated PbS-oleic acid NP as a building block. This is achieved by placing a ligated NP on each site of a face-centered lattice (conventional cell 4 distinct sites), wherein the shortest surface-to-surface separation distance between two neighboring NPs surfaces is 6 nm (Supplementary Information Figure S1). Periodic boundary conditions are employed along all directions. Note that the constructed superlattices possess a mono-disperse size distribution, i.e., all nanoparticles have identical size.

To determine the elastic properties of a given NPSL, we first equilibrate the system under ambient conditions (T = 300 K, P = 0) for 10 ns using isobaric-isothermal canonical molecular dynamics simulations using LAMMPS[43] within the CG framework described above. Constant temperature and pressure conditions are maintained using the Nosé-Hoover thermostat and barostat; a time step of 1 fs is employed. Thereafter, we employ uniaxial tensile loading along the desired crystallographic direction up to 2% strain. For a given direction, Young's modulus is evaluated from the slope of the stress-strain curves obtained from CGMD simulations. In this study, we determine Young's moduli along three crystallographic directions [100], [010], and [001] (namely E_{100}, E_{010}, E_{001} respectively). Similarly, bulk modulus K for a given NPSL is

determined from stress-strain relationship derived from CGMD simulations under isotropic strain conditions (maximum volumetric strain of 2%) Bulk modulus (K) of a given NPSL is obtained by fitting the energy to Murnaghan equation of state.[44,45] The values of Young's moduli, and bulk moduli are averaged over CGMD simulations on 10 different configurations at each ligand coverage.

Next, we investigate the response of NPSLs to applied pressure during compression-release pressure cycles using canonical molecular dynamics simulations at 300 K within LAMMPS.[43] To simulate a compression-release pressure cycle, we systematically increase applied pressure from 0 to 40 GPa in increments of 1 GPa; at each pressure, the system is equilibrated for 1 ns. Thereafter, the system pressure is gradually released at the same rate (i.e., 1 GPa/ns) down to ambient pressure. The structural and dynamical properties are all averaged over the last 200 ps for each pressure. Note that the pressure-behavior of the superlattices, and its dependence on ligand coverage presented in this work are robust, and do not exhibit any artifacts owing to computational system size; CGMD simulations on $2 \times 2 \times 2$ superlattices lead to identical results.

3. Results and discussion

Three-dimensional face centered cubic (FCC) NPSLs made up of PbS NPs (stabilized by capping with oleic acid ligands) are chosen as a representative system to investigate the role of ligand dynamics in determining the structure, elasticity, and high-pressure behavior of NPSLs. Previously, the fcc 3D NPSLs assembled from 7 nm PbS NPs have demonstrated nearly perfect structural stability upon their compression up to 12.5 GPa and further pressure release.[16] We employ CGMD simulations (see Methods and Supplementary Information Figure S1 for details) to elucidate the impact of ligand coverage on elasticity, and structural response of NPSLs to applied compression-release pressure cycles (Figure 1). The CG model and the interaction parameters employed here provides a good qualitative description of the structural and elastic behavior of NPSLs consistent with our experiments (see Supplementary Information Figure S2). A periodic simulation box comprising of four ligated NPs (at prescribed ligand coverage ρ) is used to model NPSL. A wide range of ligand coverage densities are investigated (ρ = 0.7 – 5.5

nm^{-2}); first, we focus on the structural stability, elastic behavior, and pressure response of ligand-rich NPSLs (i.e., $\rho > 1.8$ nm^{-2}), and subsequently describe the structure of ligand depleted cases. The molecular configuration of a typical FCC-NPSL ($\rho = 5.5/nm^2$) equilibrated under ambient conditions via CGMD simulations is shown in Figure 1a; in this NPSL, the shortest distance between two neighboring NPs is L = 2.8 nm. Note, ρ is defined as the number of oleic acid molecules occupying a unit area on the surface of the NP building block. Our CGMD simulations show that the elastic stiffness of NPSLs increases monotonically with ligand coverage (Figures 1b,c). This predicted trend is consistent with several earlier studies, which report that presence of thick regions of soft organic spacers between NPs (i.e., high ligand coverage) can significantly enhance the mechanical properties of NPSLs.[2,26,46] Figure 1b indicates that regardless of the ligand coverage on NP building blocks, the NPSLs exhibit elastic isotropy, as shown by largely identical values of Young's moduli along different crystallographic directions, i.e., [001], [010], and [001]. Young's moduli of NPSLs rise significantly (~1.25 to ~3 GPa) as the individual NP building block become ligand-rich (i.e., ρ increases from 1.8 nm^{-2} to 5.5 nm^{-2}), largely owing molecular-scale dynamics associated with the capping ligands as discussed later. These computed values are in good agreement with experimentally measured elastic modulus in oleic acid based NPSLs (E~ 2.3).[16,47] Similar to the trends in Young's modulus, bulk moduli K of the NPSLs also increase with ligand coverage with values in the range ~2.3 – 3.4 GPa for ρ =1.8 nm^{-2} – 5.5 nm^{-2} as shown in Figure 1c. Using CGMD simulations, we also track the structural evolution of NPSLs at various ligand coverage under applied pressure (up to 40 GPa), and during subsequent pressure release. Figure 1d shows the evolution of the surface-to-surface separation between two neighboring nanoparticles (i.e., L) in NPSLs during a compression-release cycle at various values of ρ (1.8 nm^{-2}–5.5 nm^{-2}). As expected, the inter-particle spacing L decreases under applied pressure (compression) at all ligand coverages, which are denoted by open symbols. It is interesting to note that for ρ within 1.8 nm^{-2}–5.5 nm^{-2}, the inter-particle distance in the NPSL reverts back to its original value upon complete release of pressure as shown by the filled symbols. Such a perfectly reversible structural response during a compression-release cycle is in excellent accordance with previous empirical observations.[16] This further demonstrates the capability of the coarse-grained models employed in this work to capture the behavior of NPSLs under applied pressure. To understand the effect of applied pressure on the crystalline order of the NPSLs, we evaluate the NP-NP pair

distribution function (PDF) at various points during the compression-release cycle. Figure 1e shows the NP-NP PDFs for the NPSL with ρ = 4.9 nm^{-2} at various selected pressures during a compression-release cycle. Under ambient conditions, the peaks in the NP-NP PDF appear at ideal locations for a FCC crystal, (i.e., at r_0, $\sqrt{2}r_0$, $\sqrt{3}r_0$, $2r_0$ …), where r_0 is the closest center-to-center separation between NPs (Figure 1e). As the NPSL is subjected to compression, the peaks in the PDF shift towards to shorter separation distances; however, the peak positions relative to the nearest-neighbor peak remain close to that for a FCC crystal, even up to ~40 GPa (Figure 1d). Similarly, as the applied pressure is released, the PDF peaks regain their original positions, while retaining the FCC symmetry throughout the pressure release (Figure 1d). This unique ability of NPSLs to sustain high applied pressures without losing their crystalline order is consistent with earlier experimental works.[16] It is particularly interesting to note that the qualitative trends in NP-NP PDF with applied pressure are identical for NPSLs with ligand coverages in the range 1.8 nm^{-2}–5.5 nm^{-2} [See Supporting Information Figure S3 for PDFs at ρ = 1.8 nm^{-2}, 2.4 nm^{-2}, 3.6 nm^{-2} and 5.5 nm^{-2}]. We also evaluate Steinhardt order parameters (namely, q_4 and q_6)[48,49] for the equilibrated NPSL configurations (ρ = 4.9 nm^{-2}) at various pressures during the compression-release cycle (Figures 1f,g). Consistent with the findings of PDF analysis (Figure 1e), q_4 and q_6 of the NPSL remain close to their known values for ideal FCC crystal (i.e., 0.19, and 0.57 respectively) throughout the applied compression-release cycle (Figures 1f,g). Similar to the NP-NP PDFs, the pressure dependence of Steinhardt parameters is not influenced by ligand coverage >1.8 nm^{-2}. Thus, beyond a threshold ligand coverage on NP building blocks, NPSLs can withstand high pressures while retaining their crystalline order, and exhibit completely reversible structural changes during a compression-release cycle.

In light of our simulation findings and their good agreement with the structural behavior of the NPSLs previously assembled from 7 nm PbS NPs and compressed up to 12.5 GPa,[16] we decided to experimentally assess *in situ* structural stability and mechanical properties of FCC NPSL in a much broader pressure range to estimate the validity of our computation result. Therefore, we prepared a new set of NPSLs from freshly made 7 nm PbS NPs stabilized with oleic acid (OA) using solvent/nonsolvent approach.[38] Only one NPSL was placed in a diamond anvil cell (DAC) (Figure 2a) to study its response to applied pressure under quasi-hydrostatic conditions. Structural evolution of the NPSL under applied pressure is monitored using X-ray

diffraction (XRD), and small-angle X-ray scattering (SAXS) techniques. Our synthesized NPSLs (see Materials and Methods for details) are a few to 100 μm in size (Figure 2a), making it convenient to choose a SL with dimensions compatible with the DAC (Figure 2b). Thermogravimetric analysis (TGA) shows that ligands constitute ~15% of the total weight (Figure S4) of the NPSL shown in Figure 2c; this corresponds to nearly full ligand coverage density on each constituent NP (i.e., $\rho \sim 5.0$ nm^{-2}). After loading the NPSLs into DAC (Figure 2), their structural evolution during a compression-release cycle (ambient → ~55 GPa → ambient) is investigated using SAXS (Figures 2d). Under ambient conditions, SAXS pattern displays well-defined diffraction spots analogous to single atomic crystals, thus suggesting a highly crystalline character of the superlattice (Figure 2d). Upon compression, the diffraction patterns reveal that the crystalline order is nearly perfectly preserved up to ~30 GPa. The peak positions shift to higher Q values with increasing pressure, which indicates reduction in the unit cell dimensions consistent with compression. Under applied pressure of 30--55 GPa, additional peaks appear at Q ~ 1.8 nm^{-1} while the superlattice retains its overall FCC symmetry. However, the relative intensities of the peaks change during decompression cycle that can be explained by the re-arrangement of the NPSLs . When the pressure is released back to ambient pressure, we find that the pressure-induced structural changes in NPSL revert back to original while maintain a FCC crystalline structure throughout the pressure release stage. These findings are in agreement with the previously reported structural stability demonstrated by PbS NPs upon compression up to 12.5 GPa.[16] Furthermore, it is worth noting that the all long-range order peaks broaden a little, and are less intense after pressure release, which suggests a slightly lower degree of crystalline order in the NPSL after the pressure is completely released. Figure S5 demonstrates the TEM image obtained on the fragment of NPSLs after decompression. Nevertheless, the NPSL is able to maintain its structural integrity even at elevated pressure ~ 55 GPa, consistent with the findings of our CGMD simulations (Figure 1). The high pressure studies conducted on NPSLs assembled by solvent/nonsolvent approach from 9.5 nm also confirm the stability and recovery of NPSLs during compression and pressure release cycles (Figure S6) Although our CGMD predictions are in overall agreement with experimental observations, they do not show the empirically observed slight reduction in crystallinity of NPSLs upon pressure release. This is a consequence of the superlattice sizes containing 4 NPs, which are too small to capture long-range disorder; superlattice with 16 NPs were also not found to be large enough to

capture reduction in crystallinity. Note that superlattice larger than 16 NPs (and their capping ligands) are computationally intractable.

To gain fundamental insights into the molecular origins of exceptional stiffness, reversible pressure behavior, and remarkable stability of NPSLs (at high pressures), we analyze the temporal evolution of the capping ligands in our CGMD simulations. Figure 3 shows the spatial distribution of ligands around a typical NP in face-centered cubic superlattices for various ligand coverage cases (ρ = 1.8 nm^{-2}–5.5 nm^{-2}) under ambient conditions. Initially, the ligands are placed uniformly on the surface of NPs at all ligand coverage densities (Figure 3a). During equilibration under ambient conditions (T = 300 K, P = 0), the ligands diffuse around their central NP and undergo significant re-organization. At low coverage (ρ = 1.8 nm^{-2}–3.6 nm^{-2}), the ligands re-organize into an asymmetric distribution around the central NP (Figure 3). This yields ligand-depleted regions in the interstitial space between adjacent NPs in the superlattices; which in turn, is correlated with a somewhat lower stiffness of NPSL (~1.1—1.3 GPa). Such mobility of ligands over NP surfaces has been previously reported to result in significant molecular asymmetry in the soft organic shell around NPs, even to the extent of forming self-assembled Janus-like membranes with highly anisotropic properties.[35] As the ligand coverage increases, the molecular distribution becomes uniform around a given nanoparticle. Consequently, in ligand rich NPSLs (ρ > 3.6 nm^{-2}), a soft organic shell of nearly uniform thickness forms around each NP. The presence of such soft-spacers considerably enhances the elastic stiffness of the NPSL; e.g., the Young's moduli increase by a factor of ~3 as the ligand coverage increases from 1.8 nm^{-2} to 5.5 nm^{-2} (Figures 1b). Furthermore, careful analysis of our CGMD trajectories show that the symmetry of molecular distribution around a NP is not influenced by applied pressure. Although the capping ligands undergo a range of molecular motions under applied pressure, their distribution (in a NPSL with prescribed ligand coverage) remains fairly constant during the entire compression-release cycle.

In addition to mobility and distribution of ligands around NP, the inter-digitation or the interaction between ligands tethered to neighboring NPs is a key factor controlling the structure and mechanical properties of NPSLs. We analyzed our CGMD simulation trajectories to determine the fraction of ligands involved in inter-digitation, as well as the relative orientation between ligands of different NPs in Figure 4. A ligand is considered to be involved in inter-

digitation if it contains at least two beads, each of which are within 7 Å of a bead belonging to any one of the ligands tethered to an adjacent NP (i.e., one of the 12 nearest neighbors). The ligands that do not satisfy this criterion are defined to be involved in deflection. Note the chosen cut-off distance for identifying inter-digitation (7 Å) is the nearest-neighbor separation between beads of ligands capping different NPs. Figure 4a shows the percentage of ligands involved in inter-digitation as a function of pressure over the entire compression-release cycle for NPSLs at various ligand coverages. Note that the value at each pressure in Figure 4a is averaged over 1 ns to ensure statistical relevance. At all ligand coverages, fraction of interdigitating ligands increases steadily upon compression. More importantly, during the pressure-release phase, the ligand inter-digitation reduces and reverts back to its original value upon complete release of pressure without any hysteresis. Evidently, the ligands belonging to neighboring NPs in NPSLs ($\rho > 1.8$ nm^2) interdigitate without being locked permanently (e.g., cross-linking). This reversible ligand inter-digitation underlies the complete absence of hysteresis in the structural response of NPSLs over a compression-release cycle, as well as stability at high pressures ~40 GPa (Figures 1d). Figure 4b compares the extent of inter-digitation and deflection of ligands in NPSLs at various ligand coverages under ambient conditions. NPSLs at low ligand coverages exhibit pronounced inter-digitation, while in ligand-rich NPSLs, the ligands from adjacent NPs tend to deflect away from each other. For instance, at $\rho = 1.8$ nm^{-2}, ~45% of ligands inter-digitate; the fraction of inter-digitation drops to ~30% when the ligand coverage increases to 5.5 nm^{-2}. To investigate the physical factors underlying the propensity of ligands to interdigitate or deflect away, we evaluate the angle distribution function (ADF) between the end-to-end vectors of ligands from neighboring NPs (Figure 4c; see inset for definition of angle θ between ligands). At low ligand coverages, the most probable angle value of θ determined by the maxima is ~75º. This alongside direct visualization of our CGMD trajectories reveals that at low ligand coverages, sufficient geometric space is available for the collective re-organization of ligands needed for inter-digitation (Figure 4d). As the ligand coverage increases, the steric hindrances imposed by the neighboring ligands within a given NP hinder inter-digitation and cause the ligands of neighboring NPs to bend and deflect away from each other as shown in Figure 4e. This is confirmed by the steady increase in the position of maxima in the ADF as a function of ligand coverage (Figure 4c). Beyond ρ ~3.6 nm^{-2}, the most probable value of θ shows a clear jump from ~75º to ~120º, indicating a transition from a regime dominated by ligand inter-

digitation to one in which ligands from neighboring NPs largely deflect away from each other. This transition is strongly correlated with the enhancement of elastic moduli, with somewhat low values at low ligand coverage (ligand interdigitation) to ~3 times higher moduli in the ligand rich cases (i.e., ligand deflection). Thus, we infer from Figures 1,3 and 4 that high elastic stiffness of NPSLs arise from a uniformly thick ligand shell around the inorganic NP cores, as well as high deflection of ligands in the interstitial spaces between the neighboring NPs.

The distribution of angles between the end-to-end vectors of ligands from neighboring NPs do not change appreciably with applied pressure, irrespective of the ligand coverage (Figure 4f, g). For any given ligand coverage (ρ > 1.8 nm^{-2}), the ligand-ligand ADFs remain fairly constant during the entire compression-release cycle (even up to pressures ~40 GPa). This remarkable ability of the ligands from adjacent NPs to retain their relative orientation throughout a compression-release cycle (up to ~40 GPa) enables preservation of crystalline order in NPSLs, and underlies the complete lack of hysteresis in the structural response of NPSL to applied pressure. Furthermore, the computed ADFs are broad at all ligand coverages, which provides further explanation for the isotropic elastic properties of the NPSLs considered in this work.

Finally, we investigate the structural stability of NPSLs made up of NPs whose surfaces are capped with only a few ligands. Such scenario can arise during synthesis protocols that involve extensive washing of nanoparticles.[1,35] Our CGMD simulations on NPSLs at ρ < 1.8 nm^{-2} show that ligands re-organize into small patches around the NP, while leaving large fraction of NP surfaces completely bare (Figure 5). Consequently, a significant fraction of the interstitial space between the NPs in the assembled superlattices become devoid of ligands; essentially, in these areas, the organic spacer molecules (i.e., ligands) cannot screen the NP-NP interactions. Thereby, the separation between neighboring NPs reduces, which eventually leads to sintering of NPs (Figure 5). Such ligand-deficient NPSLs cannot preserve their crystalline order at low applied pressures ~1 GPa, and often even under ambient conditions. Thus, a critical ligand coverage density ρ_c (here ~1.8 nm^{-2}) is required to form stable NPSLs. Such ligand depletion can be experimentally realized by rapid addition of an equal amount of non-solvent (i-PrOH) to toluene solution of PbS NCs and vigorous shaking. Our TGA experiments on NPSL after the non-solvent treatment shows a drop in the weight-loss, which corresponds to a reduction in the ligand coverage density (Figure 5b). SAXS experiments indicate that NPSLs lose their

crystalline order upon treatment with non-solvent (i.e., reduction in ligand coverage) as shown by pronounced broadening of peaks in the NP-NP pair distribution function (Figure 5c). These observations are consistent with predictions of our CGMD simulations. Below the critical value of ligand coverage density ρ_c, the NPs tend to aggregate or sinter; while at $\rho > \rho_c$, stable NPSLs with excellent elasticity emerge. Owing to ligand inter-digitation or deflection, these stable NPSLs ($\rho > \rho_c$) can withstand high pressures (~40 GPa) without losing their crystalline order and exhibit no hysteresis during a compression-release cycle (Figures 1d,e).

4. Conclusions

We employ CGMD simulations to elucidate the role of ligand coverage, and their molecular scale dynamics in governing the structure, elasticity, high pressure behavior of NPSLs. We find that the formation of the stable NPSLs requires the individual NP building blocks to be ligated at least up to a certain critical ligand coverage. For 7 nm PbS nanoparticles stabilized with oleic acid ligands, the critical coverage value is ~1.8 nm^{-2}. Ligand-depleted NPSLs (i.e., ligand coverage below critical value) form disordered aggregates via sintering. On the other hand, NPSLs with ligand coverages higher than the threshold value show remarkable structural stability (i.e., maintain FCC arrangement of nanocrystals) even up to high pressures, possess high elastic stiffness, and exhibit no structural hysteresis during a compression-release cycle; ligand deficiency below this threshold causes sintering of nanoparticles leading to aggregates without crystalline order. These findings can explain the disparate observations in the previously published results with some demonstrating sintering of individual NPs whereas others displaying remarkable structural stability of NPSL.[16,23] We note that this cross-over density is system specific, and may be influenced by the nature of the NP, size of the NP, ligand length and chemistries; a more systematic study would be necessary to elucidate these connections. We show that structural and mechanical properties originate from the interplay of ligand coverage, mobility, and molecular-scale dynamics of ligands in the interstitial spaces between neighboring NPs. Furthermore, ligand coverage (beyond a threshold value) can be used to tune the lattice parameter of NPSL, as well as the propensity of the ligands to inter-digitate with those tethered to a neighboring NP, or deflect away from them. Even subtle changes in the relative fraction of inter-digitated vs deflected ligands has significant impact on the mechanical behavior of NPSL; predominant ligand deflection (that occurs in ligand-rich cases) yields high elastic stiffness. The

predictions of our CGMD simulations are in good accordance with our electron microscopy, and SAXS characterization of NPSLs prepared by colloidal synthesis methods. Our work highlights the key role played by ligands in dictating the physical properties of NPSLs, provides design rules to tune these properties, and broadly advances the molecular-level understanding of NPSLs.

Conflict of interest

There are no conflicts to declare.

Acknowledgements

The authors would like to acknowledge support from the Argonne National Laboratory through the Laboratory Directed Research and Development grant LDRD-2017-012-N0. Use of the Center for Nanoscale Materials, an Office of Science user facility, was supported by the U.S. Department of Energy, Office of Science, Office of Basic Energy Sciences, under Contract No. DE-AC02- 06CH11357. B.N would also like to acknowledge support from the start-up funds at University of Louisville. This research used resources of the National Energy Research Scientific Computing Center, which is supported by the Office of Science of the U.S. Department of Energy under Contract No. DE-AC02-05CH11231. An award of computer time was provided by the Innovative and Novel Computational Impact on Theory and Experiment (INCITE) program. This research used resources of the Argonne Leadership Computing Facility at Argonne National Laboratory, which is supported by the Office of Science of the U.S. Department of Energy under contract DE-AC02-06CH11357. This research used resources of the Advanced Photon Source, a U.S. Department of Energy (DOE) Office of Science User Facility operated for the DOE Office of Science by Argonne National Laboratory under Contract No. DE-AC02-06CH11357. GeoSoilEnviroCARS is supported by the National Science Foundation—Earth Sciences (EAR-0622171) and Department of Energy—Geosciences (DE-FG02-94ER14466). Use of the Advanced Photon Source was supported by the U.S. Department of Energy, Office of Science, Office of Basic Energy Sciences, under Contract No. DE-AC02-06CH11357. We would like to thank Dr. Byeongdu Lee for insightful discussions.

References

(1) Wang, Y.; Chan, H.; Narayanan, B.; McBride, S. P.; Sankaranarayanan, S. K. R. S.; Lin, X.-M.; Jaeger, H. M. Thermomechanical Response of Self-Assembled Nanoparticle Membranes. *ACS Nano* **2017**, *11* (8), 8026–8033. https://doi.org/10.1021/acsnano.7b02676.

(2) Gu, X. W.; Ye, X.; Koshy, D. M.; Vachhani, S.; Hosemann, P.; Alivisatos, A. P. Tolerance to Structural Disorder and Tunable Mechanical Behavior in Self-Assembled Superlattices of Polymer-Grafted Nanocrystals. *Proc. Natl. Acad. Sci.* **2017**, *114* (11), 2836–2841. https://doi.org/10.1073/pnas.1618508114.

(3) Yu, D.; Wang, C.; Guyot-Sionnest, P. N-Type Conducting CdSe Nanocrystal Solids. *Science* **2003**, *300* (5623), 1277–1280. https://doi.org/10.1126/science.1084424.

(4) Shevchenko, E. V.; Ringler, M.; Schwemer, A.; Talapin, D. V.; Klar, T. A.; Rogach, A. L.; Feldmann, J.; Alivisatos, A. P. Self-Assembled Binary Superlattices of CdSe and Au Nanocrystals and Their Fluorescence Properties. *J. Am. Chem. Soc.* **2008**, *130* (11), 3274–3275. https://doi.org/10.1021/ja710619s.

(5) Collier, C. P.; Saykally, R. J.; Shiang, J. J.; Henrichs, S. E.; Heath, J. R. Reversible Tuning of Silver Quantum Dot Monolayers Through the Metal-Insulator Transition. *Science* **1997**, *277* (5334), 1978–1981. https://doi.org/10.1126/science.277.5334.1978.

(6) Courty, A.; Mermet, A.; Albouy, P. A.; Duval, E.; Pileni, M. P. Vibrational Coherence of Self-Organized Silver Nanocrystals in f.c.c. Supra-Crystals. *Nat. Mater.* **2005**, *4* (5), 395–398. https://doi.org/10.1038/nmat1366.

(7) Urban, J. J.; Talapin, D. V.; Shevchenko, E. V.; Kagan, C. R.; Murray, C. B. Synergism in Binary Nanocrystal Superlattices Leads to Enhanced P-Type Conductivity in Self-Assembled PbTe/Ag_2Te Thin Films. *Nat. Mater.* **2007**, *6* (2), 115–121. https://doi.org/10.1038/nmat1826.

(8) Sun, S.; Murray, C. B.; Weller, D.; Folks, L.; Moser, A. Monodisperse FePt Nanoparticles and Ferromagnetic FePt Nanocrystal Superlattices. *Science* **2000**, *287* (5460), 1989–1992. https://doi.org/10.1126/science.287.5460.1989.

(9) Cheon, J.; Park, J.-I.; Choi, J.; Jun, Y.; Kim, S.; Kim, M. G.; Kim, Y.-M.; Kim, Y. J. Magnetic Superlattices and Their Nanoscale Phase Transition Effects. *Proc. Natl. Acad. Sci.* **2006**, *103* (9), 3023–3027. https://doi.org/10.1073/pnas.0508877103.

(10) Dong, A.; Chen, J.; Vora, P. M.; Kikkawa, J. M.; Murray, C. B. Binary Nanocrystal Superlattice Membranes Self-Assembled at the Liquid-Air Interface. *Nature* **2010**, *466* (7305), 474–477. https://doi.org/10.1038/nature09188.

(11) Ng, K. C.; Udagedara, I. B.; Rukhlenko, I. D.; Chen, Y.; Tang, Y.; Premaratne, M.; Cheng, W. Free-Standing Plasmonic-Nanorod Superlattice Sheets. *ACS Nano* **2012**, *6* (1), 925–934. https://doi.org/10.1021/nn204498j.

(12) Black, C. T.; Murray, C. B.; Sandstrom, R. L.; Sun, S. Spin-Dependent Tunneling in Self-Assembled Cobalt-Nanocrystal Superlattices. *Science* **2000**, *290* (5494), 1131–1134. https://doi.org/10.1126/science.290.5494.1131.

(13) Boles, M. A.; Engel, M.; Talapin, D. V. Self-Assembly of Colloidal Nanocrystals: From Intricate Structures to Functional Materials. *Chem. Rev.* **2016**, *116* (18), 11220–11289. https://doi.org/10.1021/acs.chemrev.6b00196.

(14) Pileni, M.-P. Impact of the Metallic Crystalline Structure on the Properties of Nanocrystals and Their Mesoscopic Assemblies. *Acc. Chem. Res.* **2017**, *50* (8), 1946–1955. https://doi.org/10.1021/acs.accounts.7b00093.

(15) Si, K. J.; Chen, Y.; Shi, Q.; Cheng, W. Nanoparticle Superlattices: The Roles of Soft Ligands. *Adv. Sci.* **2017**, n/a-n/a. https://doi.org/10.1002/advs.201700179.
(16) Podsiadlo, P.; Lee, B.; Prakapenka, V. B.; Krylova, G. V.; Schaller, R. D.; Demortière, A.; Shevchenko, E. V. High-Pressure Structural Stability and Elasticity of Supercrystals Self-Assembled from Nanocrystals. *Nano Lett.* **2011**, *11* (2), 579–588. https://doi.org/10.1021/nl103587u.
(17) Lin, Q.-Y.; Li, Z.; Brown, K. A.; O'Brien, M. N.; Ross, M. B.; Zhou, Y.; Butun, S.; Chen, P.-C.; Schatz, G. C.; Dravid, V. P.; et al. Strong Coupling between Plasmonic Gap Modes and Photonic Lattice Modes in DNA-Assembled Gold Nanocube Arrays. *Nano Lett.* **2015**, *15* (7), 4699–4703. https://doi.org/10.1021/acs.nanolett.5b01548.
(18) Liljeroth, P.; Vanmaekelbergh, D.; Ruiz, V.; Kontturi, K.; Jiang, H.; Kauppinen, E.; Quinn, B. M. Electron Transport in Two-Dimensional Arrays of Gold Nanocrystals Investigated by Scanning Electrochemical Microscopy. *J. Am. Chem. Soc.* **2004**, *126* (22), 7126–7132. https://doi.org/10.1021/ja0493188.
(19) Kechrakos, D.; Trohidou, K. N. Magnetic Properties of Self-Assembled Interacting Nanoparticles. *Appl. Phys. Lett.* **2002**, *81* (24), 4574–4576. https://doi.org/10.1063/1.1528290.
(20) Talapin, D. V.; Murray, C. B. PbSe Nanocrystal Solids for N- and p-Channel Thin Film Field-Effect Transistors. *Science* **2005**, *310* (5745), 86–89. https://doi.org/10.1126/science.1116703.
(21) Lee, B.; Podsiadlo, P.; Rupich, S.; Talapin, D. V.; Rajh, T.; Shevchenko, E. V. Comparison of Structural Behavior of Nanocrystals in Randomly Packed Films and Long-Range Ordered Superlattices by Time-Resolved Small Angle X-Ray Scattering. *J. Am. Chem. Soc.* **2009**, *131* (45), 16386–16388. https://doi.org/10.1021/ja906632b.
(22) Ceseracciu, L.; Miszta, K.; Angelis, F. D.; Marras, S.; Prato, M.; Brescia, R.; Scarpellini, A.; Manna, L. Compression Stiffness of Porous Nanostructures from Self-Assembly of Branched Nanocrystals. *Nanoscale* **2012**, *5* (2), 681–686. https://doi.org/10.1039/C2NR32590J.
(23) Wang, T.; Li, R.; Quan, Z.; Loc, W. S.; Bassett, W. A.; Xu, H.; Cao, Y. C.; Fang, J.; Wang, Z. Pressure Processing of Nanocube Assemblies Toward Harvesting of a Metastable PbS Phase. *Adv. Mater.* **2015**, *27* (31), 4544–4549. https://doi.org/10.1002/adma.201502070.
(24) Wu, H.; Bai, F.; Sun, Z.; Haddad, R. E.; Boye, D. M.; Wang, Z.; Fan, H. Pressure-Driven Assembly of Spherical Nanoparticles and Formation of 1D-Nanostructure Arrays. *Angew. Chem. Int. Ed.* **2010**, *49* (45), 8431–8434. https://doi.org/10.1002/anie.201001581.
(25) Li, B.; Bian, K.; Zhou, X.; Lu, P.; Liu, S.; Brener, I.; Sinclair, M.; Luk, T.; Schunk, H.; Alarid, L.; et al. Pressure Compression of CdSe Nanoparticles into Luminescent Nanowires. *Sci. Adv.* **2017**, *3* (5), e1602916. https://doi.org/10.1126/sciadv.1602916.
(26) Zhu, J.; Quan, Z.; Wang, C.; Wen, X.; Jiang, Y.; Fang, J.; Wang, Z.; Zhao, Y.; Xu, H. Structural Evolution and Mechanical Behaviour of Pt Nanoparticle Superlattices at High Pressure. *Nanoscale* **2016**, *8* (9), 5214–5218. https://doi.org/10.1039/C5NR08291A.
(27) Schapotschnikow, P.; Pool, R.; Vlugt, T. J. H. Molecular Simulations of Interacting Nanocrystals. *Nano Lett.* **2008**, *8* (9), 2930–2934. https://doi.org/10.1021/nl8017862.
(28) Salerno, K. M.; Bolintineanu, D. S.; Lane, J. M. D.; Grest, G. S. High Strength, Molecularly Thin Nanoparticle Membranes. *Phys. Rev. Lett.* **2014**, *113* (25), 258301. https://doi.org/10.1103/PhysRevLett.113.258301.

(29) Waltmann, C.; Horst, N.; Travesset, A. Capping Ligand Vortices as "Atomic Orbitals" in Nanocrystal Self-Assembly. *ACS Nano* **2017**, *11* (11), 11273–11282. https://doi.org/10.1021/acsnano.7b05694.
(30) Schapotschnikow, P.; Vlugt, T. J. H. Understanding Interactions between Capped Nanocrystals: Three-Body and Chain Packing Effects. *J. Chem. Phys.* **2009**, *131* (12), 124705. https://doi.org/10.1063/1.3227043.
(31) Ye, X.; Chen, J.; Engel, M.; Millan, J. A.; Li, W.; Qi, L.; Xing, G.; Collins, J. E.; Kagan, C. R.; Li, J.; et al. Competition of Shape and Interaction Patchiness for Self-Assembling Nanoplates. *Nat. Chem.* **2013**, *5* (6), 466–473. https://doi.org/10.1038/nchem.1651.
(32) Castelli, A.; Graaf, J. de; Marras, S.; Brescia, R.; Goldoni, L.; Manna, L.; Arciniegas, M. P. Understanding and Tailoring Ligand Interactions in the Self-Assembly of Branched Colloidal Nanocrystals into Planar Superlattices. *Nat. Commun.* **2018**, *9* (1), 1141. https://doi.org/10.1038/s41467-018-03550-z.
(33) Wang, Z.; Schliehe, C.; Bian, K.; Dale, D.; Bassett, W. A.; Hanrath, T.; Klinke, C.; Weller, H. Correlating Superlattice Polymorphs to Internanoparticle Distance, Packing Density, and Surface Lattice in Assemblies of PbS Nanoparticles. *Nano Lett.* **2013**, *13* (3), 1303–1311. https://doi.org/10.1021/nl400084k.
(34) Landman, U.; Luedtke, W. D. Small Is Different: Energetic, Structural, Thermal, and Mechanical Properties of Passivated Nanocluster Assemblies. *Faraday Discuss.* **2004**, *125* (0), 1–22. https://doi.org/10.1039/B312640B.
(35) Jiang, Z.; He, J.; Deshmukh, S. A.; Kanjanaboos, P.; Kamath, G.; Wang, Y.; Sankaranarayanan, S. K. R. S.; Wang, J.; Jaeger, H. M.; Lin, X.-M. Subnanometre Ligand-Shell Asymmetry Leads to Janus-like Nanoparticle Membranes. *Nat. Mater.* **2015**, *14* (9), 912–917. https://doi.org/10.1038/nmat4321.
(36) Wu, H.; Bai, F.; Sun, Z.; Haddad, R. E.; Boye, D. M.; Wang, Z.; Huang, J. Y.; Fan, H. Nanostructured Gold Architectures Formed through High Pressure-Driven Sintering of Spherical Nanoparticle Arrays. *J. Am. Chem. Soc.* **2010**, *132* (37), 12826–12828. https://doi.org/10.1021/ja105255d.
(37) Hines, M. A.; Scholes, G. D. Colloidal PbS Nanocrystals with Size-Tunable Near-Infrared Emission: Observation of Post-Synthesis Self-Narrowing of the Particle Size Distribution. *Adv. Mater.* **2013**, *15* (21), 1844–1849. https://doi.org/10.1002/adma.200305395.
(38) Shevchenko, E.; Talapin, D.; Kornowski, A.; Wiekhorst, F.; Kötzler, J.; Haase, M.; Rogach, A.; Weller, H. Colloidal Crystals of Monodisperse FePt Nanoparticles Grown by a Three-Layer Technique of Controlled Oversaturation. *Adv. Mater.* **2002**, *14* (4), 287–290. https://doi.org/10.1002/1521-4095(20020219)14:4<287::AID-ADMA287>3.0.CO;2-6.
(39) Koo, B.; Xiong, H.; Slater, M. D.; Prakapenka, V. B.; Balasubramanian, M.; Podsiadlo, P.; Johnson, C. S.; Rajh, T.; Shevchenko, E. V. Hollow Iron Oxide Nanoparticles for Application in Lithium Ion Batteries. *Nano Lett.* **2012**, *12* (5), 2429–2435. https://doi.org/10.1021/nl3004286.
(40) Marrink, S. J.; Risselada, H. J.; Yefimov, S.; Tieleman, D. P.; de Vries, A. H. The MARTINI Force Field: Coarse Grained Model for Biomolecular Simulations. *J. Phys. Chem. B* **2007**, *111* (27), 7812–7824. https://doi.org/10.1021/jp071097f.
(41) Baron, R.; de Vries, A. H.; Hünenberger, P. H.; van Gunsteren, W. F. Comparison of Atomic-Level and Coarse-Grained Models for Liquid Hydrocarbons from Molecular Dynamics Configurational Entropy Estimates. *J. Phys. Chem. B* **2006**, *110* (16), 8464–8473. https://doi.org/10.1021/jp055888y.

(42) José Dalmaschio, C.; Firmiano, E. G. da S.; Narcisio Pinheiro, A.; Guedes Sobrinho, D.; Moura, A. F. de; Roberto Leite, E. Nanocrystals Self-Assembled in Superlattices Directed by the Solvent –Organic Capping Interaction. *Nanoscale* **2013**, *5* (12), 5602–5610. https://doi.org/10.1039/C3NR00883E.
(43) Plimpton, S. Fast Parallel Algorithms for Short-Range Molecular Dynamics. *J. Comput. Phys.* **1995**, *117* (1), 1–19. https://doi.org/10.1006/jcph.1995.1039.
(44) Murnaghan, F. D. The Compressibility of Media under Extreme Pressures. *Proc. Natl. Acad. Sci. U. S. A.* **1944**, *30* (9), 244–247.
(45) Narayanan, B.; Reimanis, I. E.; Fuller, E. R.; Ciobanu, C. V. Elastic Constants of $\ensuremath{\beta}$-Eucryptite Studied by Density Functional Theory. *Phys. Rev. B* **2010**, *81* (10), 104106. https://doi.org/10.1103/PhysRevB.81.104106.
(46) Salerno, K. M.; Bolintineanu, D. S.; Lane, J. M. D.; Grest, G. S. Ligand Structure and Mechanical Properties of Single-Nanoparticle-Thick Membranes. *Phys. Rev. E* **2015**, *91* (6), 062403. https://doi.org/10.1103/PhysRevE.91.062403.
(47) Tam, E.; Podsiadlo, P.; Shevchenko, E.; Ogletree, D. F.; Delplancke-Ogletree, M.-P.; Ashby, P. D. Mechanical Properties of Face-Centered Cubic Supercrystals of Nanocrystals. *Nano Lett.* **2010**, *10* (7), 2363–2367. https://doi.org/10.1021/nl1001313.
(48) Steinhardt, P. J.; Nelson, D. R.; Ronchetti, M. Bond-Orientational Order in Liquids and Glasses. *Phys. Rev. B* **1983**, *28* (2), 784–805. https://doi.org/10.1103/PhysRevB.28.784.
(49) Mickel, W.; Kapfer, S. C.; Schröder-Turk, G. E.; Mecke, K. Shortcomings of the Bond Orientational Order Parameters for the Analysis of Disordered Particulate Matter. *J. Chem. Phys.* **2013**, *138* (4), 044501. https://doi.org/10.1063/1.4774084.

FIGURES AND TABLES

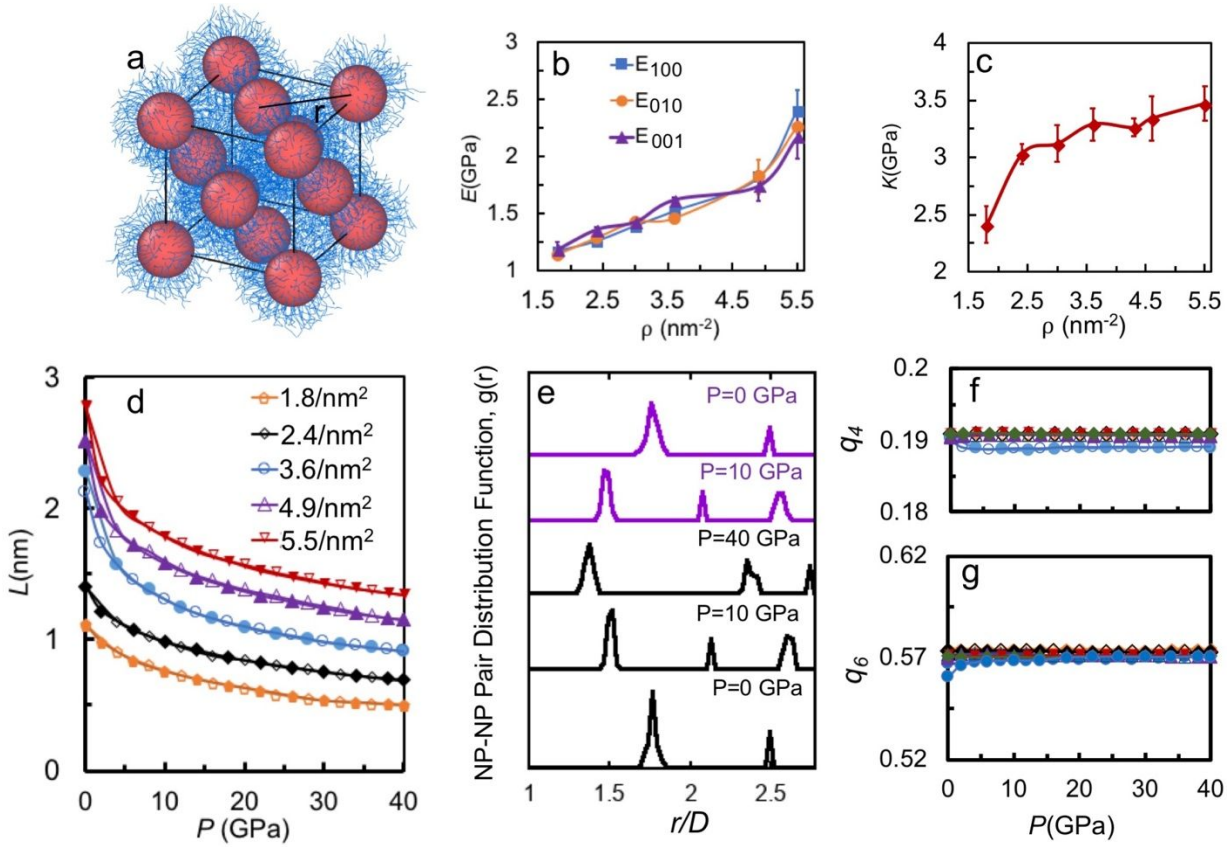

Figure 1. Coarse-grained molecular dynamics simulations to understand structural and mechanical properties of NPSLs at various ligand coverages. (a) CG model representation of a typical face-centered cubic NPSL. The NPs are shown as red spheres, while the ligands are shown as blue lines. The distance between the center of masses of two neighboring NPs are denoted as r; while, the surface-to-surface distance between neighboring NPs can be written as $L = r - D$, where D is the diameter of each NP. (b) Young's modulus of NPSL along three different crystallographic directions, [100], [010] and [001], namely E_{100}, E_{010}, E_{001} are plotted as a function of ligand coverage ρ. (c) Bulk modulus of NPSL at various values of ρ. The values in panels (b, c) are averaged over 10 different configurations; error bars are also provided (d) Average surface-to-surface separation distance between adjacent NPs in equilibrated NPSLs for different ligand coverages as a function of pressure P during a compression-release cycle. Here D is the diameter of a nanoparticle. Here, the open and filled symbols correspond to compression and pressure-release phases of the cycle, respectively. (e) Pair distribution function between NPs for a NPSL at ρ=4.9/nm^2 at various selected pressures during a compression-release cycle. (f, g) Steinhardt order parameter q_4 and q_6 for NPSL (ρ=4.9/nm^2) at selected pressures chosen in panel (e). Open and filled symbols correspond to the compression and pressure release phases, respectively, in panels (d, f, g). Similarly, in panel e, the PDFs during compression are shown in black, while that for the release of pressure are displayed in purple.

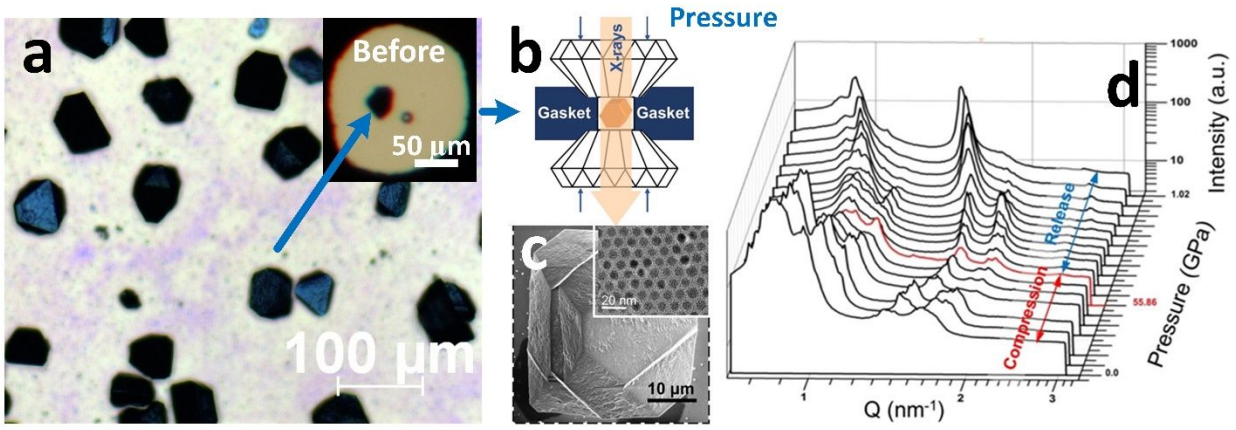

Figure 2. Experimental characterization of the high-pressure behavior of face-centered cubic NPSLs made up of 7 nm PbS nanoparticles. (a) Optical micrograph of the PbS NPSLs deposited on the Si substrate and individual NPSL loaded into DAC (insert). Schematic representation of the diamond-anvil cell set-up used for in-situ X-ray characterization of NPSL. (c) Scanning electron microscopy image of NPSL, the inset demonstrates the TEM image of 7 nm PbS NPs used to make 3D NPSL. (d) Evolution of SAXS spectra for the NPSL as a function of applied pressure during a compression-release cycle. The red line indicates the SAXS spectra at the highest pressure achieved (55.86 GPa). The acquisition of the data starts at 1.02 GPa and the data are compared to the diffraction spectrum of SCs on Si substrate. 2D XRD patterns showing preferential orientation of NPs in the NPSL are shown during compression (panels d,e) and upon release (panel f).

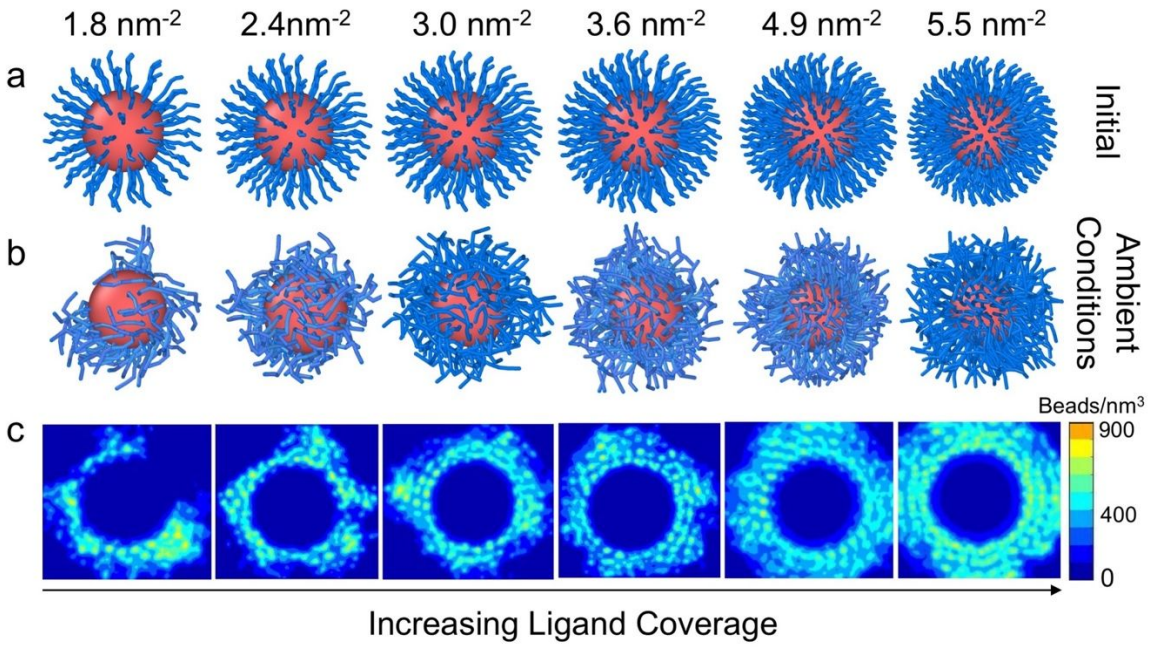

Figure 3. Distribution of ligands around a typical nanoparticle in a NPSL at various ligand coverages under ambient conditions. Molecular snapshots of capping ligands on a NP within the NPSL are shown (a) initially, when they are uniformly placed, and (b) after equilibration of NPSLs under ambient conditions (P = 0, T = 300 K) via CGMD simulations. (c) Time-averaged number density maps showing the distribution of ligands around a typical nanoparticle within the NPSL at various ligand coverages are also shown. The color bar represents number of ligand beads per unit volume (nm^{-3}).

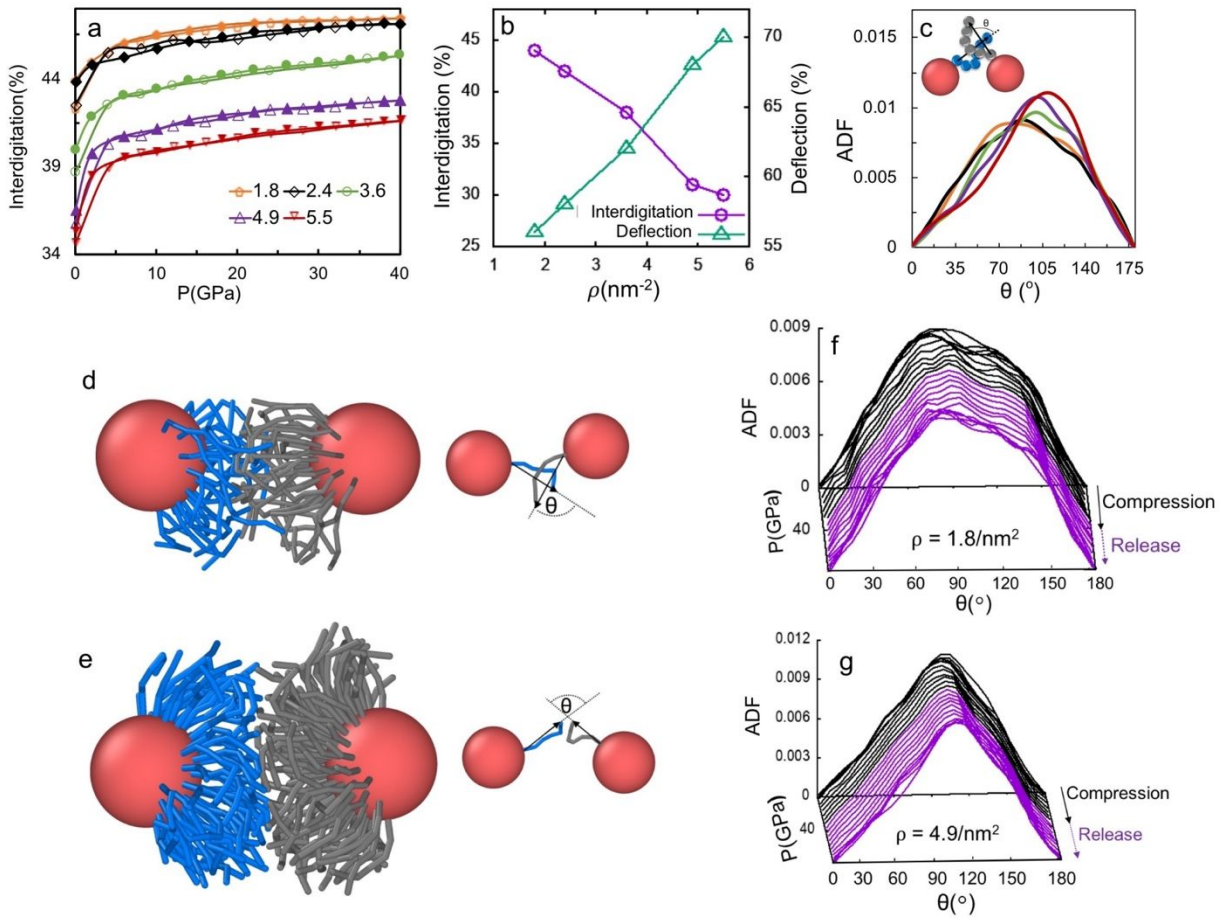

Figure 4. Interaction between ligands belonging to neighboring nanoparticles. (a) Fraction of ligands involved in interdigitation in NPSLs at various ligand coverages as a function of pressure during a compression-release cycle. Open and closed symbols correspond to compression and release phases respectively. (b) Fraction of ligands involved in interdigitation and deflection under ambient conditions as a function of ligand coverage. (c) Probability distribution of angles (ADF) between the end-to-end vectors of ligand pairs (each tethered to a different NP) under ambient conditions for various ligand coverage densities. The angle θ between the ligands is defined in the inset. Molecular snapshots of a pair of selected NPs (red spheres) exhibiting predominant (d) interdigitation, and (e) deflection of ligands (blue lines) in the interstitial region, obtained from CGMD trajectories. Only ligands that lie between the chosen NPs are shown for clarity. All the ligands belonging to a single nanoparticle are of same color (blue or gray lines). The angle between the edge-to-edge vectors of a representative pair of ligands for each case in panels (d, e) are also shown to illustrate their relative orientation. We have also shown the probability distribution of angles between ligands of different NPs for (f, g) ligand-deficient (ρ = 1.8 nm^{-2}) and ligand-rich (ρ = 5.5 nm^{-2}) NPSLs as a function of pressure during a compression-release cycle.

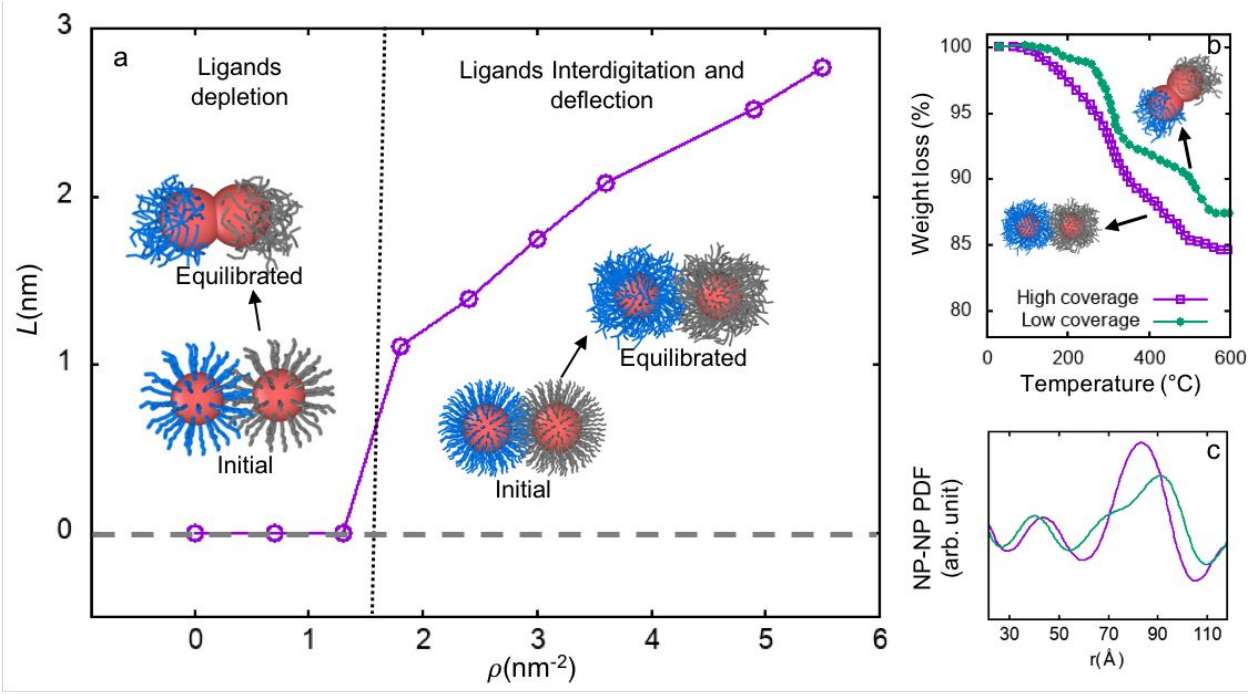

Figure 5. Ligand coverage effects on the morphology of NPSL. (a) Surface-to-surface separation distance between neighboring nanoparticles L in face-centered cubic NPSLs as a function of ligand coverage under ambient conditions as obtained from our CGMD simulations. Two distinct regimes in structural behavior appear, which are separated by a dotted line. At $\rho < 1.8$ nm^{-2}, the NPs tend to sinter leading to loss of order in the NPSL. Beyond 1.8 nm^{-2}, NPSLs are stable even under high applied pressures ~40 GPa. Within this regime, the extent of ligand interdigitation varies with coverage density; as ρ increases, ligands belonging to neighboring NPs tend to deflect away from each other. Representative molecular snapshots are shown for each regime to demonstrate that ligand re-organization leads to 1) sintering of NPs and consequent collapse of long-range order (in ligand-depleted NPSLs), and 2) interdigitation, and/or deflection of ligands in the interstitial space between adjacent NPs that underlie the structural stability of ligand-rich NPSL. (b) Thermogravimetric analysis (*cf.* Reference 19) of a PbS NPSL, and disordered structures obtained by treating crystalline NPSL with non-solvent. TGA weight loss is used to ascertain the coverage; low coverage of NP leads to a disordered *i.e.* sintered aggregate, whereas the NPSL with higher coverage maintained its crystallinity. These experimental observations are consistent with our simulations. (c) Pair-distribution functions of these NPSLs obtained from SAXS experiments; broadening of peaks in the films with lower coverage indicate disorder whereas the higher coverage films maintain their structural integrity.

Graphical abstract